AGU PUBLICATIONS

JGR

Journal of Geophysical Research: Solid Earth

RESEARCH ARTICLE

10.1002/2013JB010904

Key Points:
- Observation of stable resonances during two microseismic experiments
- Analysis of source, path, and receiver effects associated with each experiment
- Resonances might correspond to mesoscale deformation or nonlaminar fluid flow

Correspondence to:
J. B. Tary,
tary@ualberta.ca

Citation:
Tary, J. B., M. van der Baan, and D. W. Eaton (2014), Interpretation of resonance frequencies recorded during hydraulic fracturing treatments, *J. Geophys. Res. Solid Earth*, *119*, 1295–1315, doi:10.1002/2013JB010904.

Received 5 DEC 2013
Accepted 27 JAN 2014
Accepted article online 4 FEB 2014
Published online 25 FEB 2014

Interpretation of resonance frequencies recorded during hydraulic fracturing treatments

J. B. Tary[1], M. van der Baan[1], and D. W. Eaton[2]

[1]Department of Physics, University of Alberta, Edmonton, Alberta, Canada [2]Department of Geoscience, University of Calgary, Calgary, Alberta, Canada

Abstract Hydraulic fracturing treatments are often monitored by strings of geophones deployed in boreholes. Instead of picking discrete events only, we here use time-frequency representations of continuous recordings to identify resonances in two case studies. This paper outlines an interpretational procedure to identify their cause using a subdivision into source, path, and receiver-side effects. For the first case study, two main resonances are observed both at depth by the downhole geophones and on the surface by two broadband arrays. The two acquisition networks have different receiver and path effects, yet recorded the same resonances; these resonances are therefore likely generated by source effects. The amplitude pattern at the surface arrays indicates that these resonances are probably due to pumping operations. In the second case study, selective resonances are detected by the downhole geophones. Resonances coming from receiver effects are either lower or higher frequency, and wave propagation modeling shows that path effects are not significant. We identify two possible causes within the source area, namely, eigenvibrations of fractures or non-Darcian flow within the hydraulic fractures. In the first situation, 15–30 m long fluid-filled cracks could generate the observed resonances. An interconnected fracture network would then be required, corresponding to mesoscale deformation of the reservoir. Alternatively, systematic patterns in non-Darcian fluid flow within the hydraulic fracture could also be their leading cause. Resonances can be used to gain a better understanding of reservoir deformations or dynamic fluid flow perturbations during fluid injection into hydrocarbon and geothermal reservoirs, CO_2 sequestration, or volcanic eruptions.

1. Introduction

Hydraulic fracturing aims to increase the reservoir permeability by opening fractures, thereby facilitating drainage of hydrocarbons or fluid circulation in engineered geothermal systems [*van der Baan et al.*, 2013]. While fluid injection is taking place, microseismic events are generated by the reactivation of preexisting fractures and the creation of new fractures. The fracturing process is usually monitored by geophones deployed in one or more boreholes (Figure 1). Using these instruments to locate the microseismicity, the stimulated reservoir volume is assumed to correspond to the zone covered by the microseismic cloud when dealing with tight hydrocarbons. Therefore, microseismic monitoring depends mainly on brittle failure to estimate reservoir deformation [*van der Baan et al.*, 2013], even if new techniques are being developed to enhance microseismic monitoring such as time-lapse seismic tomography [*Calo et al.*, 2011] or interferometry [*de Ridder and Dellinger*, 2011; *Grechka and Zhao*, 2012].

Yet the total input energy corresponding to the injected fluid is orders of magnitude larger than the estimated energy coming from the recorded microseismic events [*Maxwell et al.*, 2009]. The energy dissipated by fluid leak-off and friction within the well and the reservoir does not account for this discrepancy. Apart from brittle failure, other types of deformation must take place in the reservoir to release the extra energy, like tensile fracturing and slow aseismic deformation [*Chorney et al.*, 2012]. Conventional processing uses triggered events to monitor hydraulic fracturing treatments. However, slow deformation and more generally long-duration phenomena may not be detected by this procedure as they usually have emergent onsets [*Bame and Fehler*, 1986; *Das and Zoback*, 2013].

Unconventional events and resonance frequencies have been studied using time-frequency representations of continuous passive recordings. For example, Long-Period and Long-Duration events (LPLD) are detected after band passing the recorded data based on the frequency content of the different observed signals (microseismic events, ambient noise...) obtained using the Short-Time Fourier Transform (STFT) [*Das*

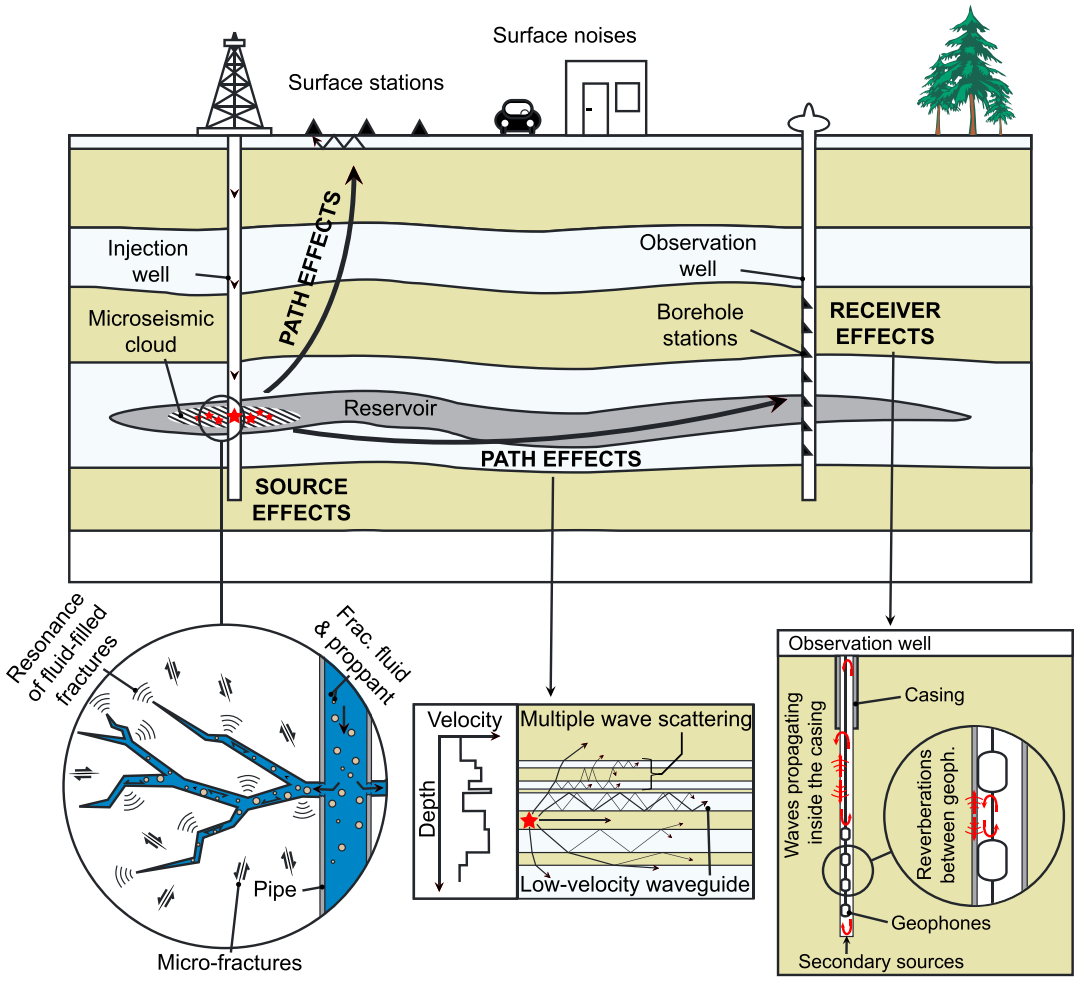

Figure 1. Sketch of a typical configuration of hydrofracture experiments. Seismic waves generated by fracturing or perforation shots (red stars) travel through the Earth (reservoir and other geological formations) and are eventually recorded by seismic stations located either on the surface or in an observation well. Insets show sketches illustrating the source, path, and receiver effects. At the receiver side, resonances may occur from reverberations between receivers or within the entire borehole. Likewise, source effects can include wave reverberations within fracture networks or vibrations from fluids leaving the well through small perforations. The different parts of the borehole and the fluid-filled fracture are not at the right scale, as the borehole radius is ~5–12 cm, and the fracture thickness and length are only a few millimeters and few meters to few tens of meters, respectively. For the path effects, the seismic waves generated by a source (red star) travel through layers with different velocities. These waves will be reflected and transmitted at layer boundaries or can be trapped in a low-velocity waveguide. Modified from *Tary and van der Baan* [2012].

and Zoback, 2011]. Likewise, *Pettitt et al.* [2009] try to incorporate in a single framework the microseismicity, hydraulic treatment conditions, and data frequency content. They observe resonance frequencies during and between microseismic experiments with variations in amplitude. For one stage, while some microseismicity is directly associated with the fluid injection close to the well, some microseismic events occur near jointly in an upper formation implying a possible fluid communication between the two formations. No microseismicity is observed between the upper and injection formations. On the other hand, the frequency content shows a decrease in amplitude over time of some of the high-frequency resonances at that time. *Pettitt et al.* [2009] interpret this observation as the slow growth of a fracture by the agglomeration of microfractures going from the lower to upper level, without sufficient instantaneous slip or fracturing to generate a recordable microseismic event in the intermediate formation.

As shown by these studies, the frequency content of continuous recordings contains useful information for preprocessing the data as well as useful clues for understanding reservoir deformation. Time-frequency representations are particularly appropriate to study long-lasting phenomena with localized frequency contents.

In this paper we outline an interpretational strategy to identify the cause of any observed resonances. Although the focus is on hydraulic fracture treatments, the developed framework is applicable to all situations involving fluid intrusion into a surrounding rock including geothermal operations but possibly also volcanology applications.

A seismic signal is usually seen as the convolution of the contribution of source, path, and receiver effects (Figure 1). Different resonant peaks can be introduced by all these effects. Fortunately, resonances coming from different sources are usually also characterized by different spectral peaks and can thus be separated. Following the identification of resonances using suitable time-frequency methods, the next step is then to identify the possible causes of resonance frequencies using this categorization into source, receiver, and path effects.

We then present two case studies with clear resonance frequencies. In both cases, we first try to locate the cause of the resonances by estimating the moveout of wave packets and/or wave polarization analysis. We isolate the influence of receiver, path, and source effects to discuss the potential causes of the resonances. We end with a discussion on the most likely implications for the observed resonances in terms of either reservoir deformation and a growing hydraulic fracture, or fluid flow effects within the hydraulic fracture.

2. Causes of Resonance Frequencies

This section reviews various causes for the existence of resonance frequencies in order to create an interpretational framework to establish the most likely cause for any observed resonances in case of fluid injection into a hydrocarbon or geothermal reservoir.

2.1. Receiver Effects

In receiver effects, we are including contributions from the instrument itself and the observation well where the sensors are deployed to monitor microseismic experiments. Generally, the resonances introduced on the receiver side are directly related to the experimental setup. First, mechanical resonances sometimes corrupt the data when the internal damping or the clamping of the sensors is flawed. Surface stations are sometimes buried at few tens of meters to avoid contamination from anthropogenic and environmental noises, as well as wave trapping in the unconsolidated soil layer.

During hydraulic fracturing treatments, geophones are typically deployed in an observation well few hundreds to few thousands of meters deep. The resulting decrease in noise level is important to detect the very small microseismic events ($-4 < M_w < -1$) generated during the fluid injection. On the other hand, noises can be generated by the trapping of waves (tube and *P* waves) inside the fluid-filled pipe (Figure 1) [*Sun and McMechan*, 1988]. The resonance frequencies are generated by constructive interferences of a fundamental wave mode given by the fluid (generally water) or casing velocity divided by the length of the pipe. Likewise, any discontinuities within the borehole such as collars and tubing ends may reflect the internal waves, potentially creating additional resonances. In some instances, geophones are shown to generate resonances due to their strong clamping on the pipe, the frequency depending on the casing velocity and the geophone spacing [*St-Onge and Eaton*, 2011]. Interestingly, the fluid pressure inside the borehole may change the corresponding resonance frequency by deforming the pipe itself [*St-Onge et al.*, 2013]. Thus, changes of resonance frequency may correlate with the injection rate during the fluid injection.

2.2. Path Effects

Resonance frequencies resulting from path effects have been extensively studied, yet they are still not fully understood due to the reality of the Earth's complexity. In the case of seismic hazard assessment in urban areas, for example, resonances introduced by site effects arise mainly from the constructive and destructive interferences of waves due to topography or low-velocity waveguides [e.g., *Bonnefoy–Claudet et al.*, 2006; *van der Baan*, 2009]. In the latter case, the resonant peaks depend directly on the mechanical properties of the low-velocity layers, including the impedance contrast and the thickness of these layers. To estimate the position of the resonances, the main tools are the spectral ratio method developed by *Nakamura* [2000] and the quarter-wavelength law [*van der Baan*, 2009]. Reservoirs containing oil or gas constitute sometimes low-velocity layers and could, in principle, be characterized by a specific resonance frequency.

Another way for path effects to introduce resonances is via multiple wave scattering along the path between source and receiver. This phenomenon, also called stratigraphic filtering, depends on the layers reflectivity and the wavelength of the various propagating waves. It has been studied by using deterministic and

stochastic approaches. The deterministic approach is employed in the case of periodic, or quasi-periodic media [*Morlet et al.*, 1982a, 1982b]. It shows that, for long wavelengths, the medium is effectively homogeneous and characterized by an averaged velocity, and for short wavelengths, waves are strongly attenuated creating "forbidden bands." A periodic stratification can then act as a low-pass or a pass-band filter, hence, the name stratigraphic filtering.

In the stochastic approach using the wave localization theory, the medium is defined by a stack of layers with stochastic velocity variations sandwiched by two homogeneous half spaces. Contrary to the deterministic approach where the medium is known perfectly, the stochastic approach uses statistical values derived from spatial autocorrelation functions with a given standard deviation in velocity fluctuations to predict resulting frequency-dependent attenuation and dispersion [*van der Baan*, 2001; *van der Baan et al.*, 2007]. Stratigraphic filtering can then act as a low-pass filter, or when the characteristic scale length of the medium is close to the principal wavelength, wave localization occurs and scattered waves interact constructively to create resonances [*Banik et al.*, 1985; *Correig and Vila*, 1993; *van der Baan et al.*, 2007]. All the abovementioned causes of resonances due to path effects can be studied using wave propagation modeling and proper model parameters.

2.3. Source Effects

On the source side, resonance frequencies might be introduced by surface noises related to the pumping operations. They can also arise from the repetition of small, periodic events [*Lees et al.*, 2004; *Pettitt et al.*, 2009]. The succession of these small events would appear as a line at a frequency inversely proportional to the interevent period. During hydraulic fracturing, small events could correspond to microfractures of too small amplitudes to be identified as individual events. Changes in resonance frequencies could be produced by variations in the periodicity of the small repetitive events [*Hotovec et al.*, 2013].

In many respects, hydraulic fracturing is similar to magma migration in the subsurface [*Bame and Fehler*, 1986; *Ferrazzini et al.*, 1990]. In this context, resonance frequencies and low-frequency events are often interpreted as the resonance of fluid-filled cracks at depth [*Aki et al.*, 1977; *Chouet*, 1986]. Using a model with a rectangular crack embedded in an elastic solid and filled by nonviscous fluid, *Chouet* [1986] shows that the crack resonance is sustained by the propagation of a dispersive wave with a very low velocity at the fluid-solid interface. The frequency response of the crack itself is mainly affected by the triggering excitation (size, source function, and location), the crack dimensions, and the mechanical parameters of the model through the crack stiffness parameter [*Aki et al.*, 1977; *Chouet*, 1986]. The existence of the slow wave has since been confirmed experimentally [*Tang and Cheng*, 1988; *Goloshubin et al.*, 1994] and studied by many authors [e.g., *Yamamoto and Kawakatsu*, 2008; *Frehner and Schmalholz*, 2010]. Following *Korneev* [2011], we hereafter refer to this wave as a Krauklis wave.

The dispersion curve of the phase velocity of this wave has been derived analytically by *Ferrazzini and Aki* [1987] and *Korneev* [2008], for an infinite fluid-filled crack sandwiched between two elastic half spaces. The velocity of Krauklis waves tends toward zero at zero frequency and becomes a nondispersive Scholte wave at high frequencies [*Korneev*, 2011]. Tube waves on the contrary, are propagating as plane waves in the fluid at low frequencies and as dispersive Stoneley waves at the pipe-formation interface at high frequencies [*Rama Rao and Vandiver*, 1999].

Resonance frequencies generated by Krauklis wave reverberations in a fluid-filled fracture with flat tips and uniform properties are given by equation (A3) (see Appendix A). In reality, the thickness of the fracture is likely to change along its course, in particular at the tip, where the thickness decreases progressively [*Rubin*, 1995]. The fracture thickness in equation (A3) is then an average thickness over the total length of the fracture. For instance, a linear pinch-out model for a fracture increases the travel time in the fracture by a factor of $\frac{3}{2}$ (V. Korneev, personal communication, 2013, see Appendix A). This travel time increase decreases the resonance frequency by a factor $\frac{2}{3}^{\frac{3}{2}}$ (equation (A6)).

During the fluid injection, various resonances can arise from fluid-filled fractures depending on fracture growth and collapse or the fluid properties. In particular, the fluid pressure can change the dispersion curve of Krauklis waves [*Nagano and Niitsuma*, 2000], changing the resonance frequencies. The proppant concentration might also have a significant influence.

Possible pressure variations triggering the resonance of a fracture/conduit may arise from various causes, most of them being relevant for both volcanoes and hydraulic stimulations. Brittle failure leading to

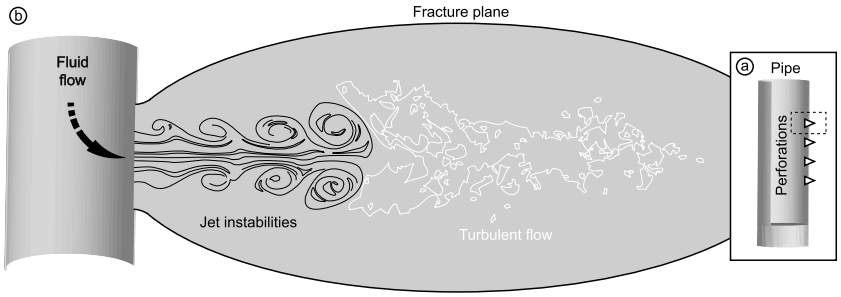

Figure 2. Illustration of nonlaminar flow model for the generation of resonance frequencies by Orr-Sommerfeld instabilities. As the fluid enters the fracture through the (a) perforation(s), the high-speed fluid flow involves the production of periodic pressure variations due to small-scale vortices along the (b) fluid flow creating resonance frequencies. Perforations are openings in the pipe casing usually between 0.005 and 0.01 m, while the pipe diameter is generally around 0.05–0.1 m. This mechanism may take place at other locations due to fracture restrictions, for example. Jet instabilities are modified from *Van Dyke* [1982].

fracture extension involves a sudden depressurization in the fluid and conversely for fracture collapse [*Aki et al.*, 1977; *Chouet*, 1988; *Shimomura et al.*, 2006]. The pressure-induced opening and closing of cracks can produce complex source spectra in individual events, including spectral notches which have been observed in the first case study considered below recorded over a hydraulic fracturing treatment [*Eaton et al.*, 2014]. The resulting seismic events can also excite resonances in the conduit if located close to its walls [*Neuberg et al.*, 2006; *Shimomura et al.*, 2006; *Thomas and Neuberg*, 2012], similarly to seismic waves trapped in low-velocity waveguides [*van der Baan*, 2009]. Sudden changes in temperature at depth can also lead to fracturing, such as during magma or hydrothermal fluid intrusion in volcanoes [*Burlini et al.*, 2007; *Konstantinou and Schlindwein*, 2003] or steam injection in reservoirs [*Chopra et al.*, 2010; *Maxwell et al.*, 2007]. Fluid movements can induce pressure variations through sudden inflow or outflow [*Ferrick et al.*, 1982; *Chouet et al.*, 2005; *Lesage et al.*, 2006; *De Barros et al.*, 2011] or due to overall unsteady fluid flow [*Ferrick et al.*, 1982; *Rust et al.*, 2008]. Fluid-phase transitions (liquid-gas-supercritical fluid) due to changes in in situ conditions or during fluid migration toward the surface also generate rapid pressure variations that could trigger crack resonances [*Bohnhoff and Zoback*, 2010; *Maeda et al.*, 2013].

Volcanic tremors and low-frequency events can also be produced by fluid flow instabilities [e.g., *Ferrick et al.*, 1982; *Julian*, 1994; *Rust et al.*, 2008]. A first indication of whether or not the conditions for non-Darcian (i.e., nonlaminar) flow are met is given by the Reynolds number, which represents the ratio of inertial to viscous forces. The Reynolds number is given by $Re = \frac{\rho_f v D}{\mu_d}$, where v is the fluid flow velocity, D the characteristic size of the opening, ρ_f the density of the fluid and μ_d the dynamic viscosity. Fluid injection during hydraulic stimulation generally involves high Reynolds number with high fluid flow velocities. Non-Darcian flow is not uncommon in hydraulic fracturing treatments at the perforation location or the fracture system [*Evans et al.*, 1996; *Kohl et al.*, 1997; *Quinn et al.*, 2011]. Several mechanisms for the generation of resonances relevant in these conditions have been suggested by *Hellweg* [2000] (eddy shedding, periodic appearance of turbulent flow) and *Rust et al.* [2008] (fluid flow instabilities similar to Roll waves, reservoir resonance analogous to a Helmholtz resonator). Resonance frequencies associated with each mechanism depend mainly on the fluid flow velocity and some characteristic geometrical dimensions.

The crack model seems to require opposite conditions to fluid flow models, as the first requires finite cracks to generate resonances, and the latter requires an open channel and continuous flow. The fluid flow model may be more applicable at the perforation location where fluids are channeled into the expanding hydraulic fracture (Figure 2), whereas the resonating crack model may be more applicable further along the (expanding) hydraulic fracture.

3. Observed Resonances

In the following we present two case histories illustrating how the most likely cause of observed resonances can be identified using the division into source, receiver, and path effects.

3.1. Case Study 1

The first case study uses a microseismic data set collected in Rolla, northeastern British Columbia, in 2011 (Figure 3). The main target play in this area is the lower-triassic Montney formation. The Montney formation,

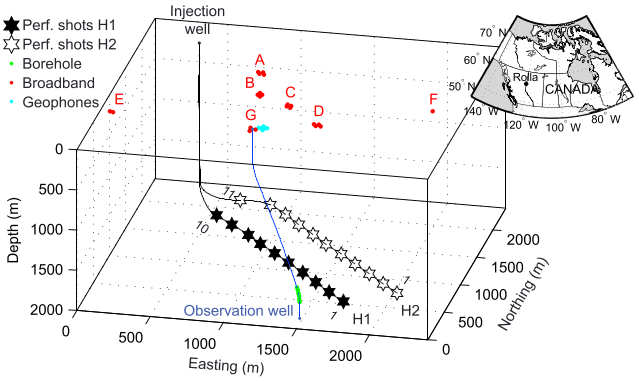

Figure 3. Experimental setup of the Rolla experiment. The perforation shots are indicated by black and open stars for the first (H1) and second (H2) well, respectively. The perforation shot numbers are also shown close to the stars. The downhole geophones are indicated by green dots, the broadband stations by red dots, and the geophones on the surface by light blue dots.

present from west-central Alberta to northeastern British Columbia, contains important conventional gas and oil reserves as well as unconventional tight gas and shale gas mainly in British Columbia [*National Energy Board*, 2009; *Zonneveld et al.*, 2010]. The formation comprises mainly shale and silty shale but also contains beds of siltstone and sandstone [*Dixon*, 2000].

Twenty-one stages were carried out in two horizontal wells, H1 and H2, having the vertical section in common (Figure 3). The fluid injection was monitored by a downhole array of six modified short-period geophones (natural frequency of 4.5 Hz, noise floor between 0.1 and 1 Hz), and by 21 broadband stations (frequency band ~0.01–100 Hz) and eight geophones (natural frequency of 10 Hz) on the surface. The downhole geophones were deployed at depths ranging from 1670 to 1830 m and were approximately 100 m above the horizontal portion of the injection well. During the fracturing stages of well H1, no data could be retrieved from two of the geophones (1 and 6). Further details on this experiment can be found in *Eaton et al.* [2013].

About 70 microseismic events are detected and located using the geophones deployed in the observation well, whereas no microseismic event is detected by the sensors on the surface. Their moment magnitudes range from −2 to −0.4. Except for these high-frequency events, some low-frequency transient events (<25 Hz, *Eaton et al.* [2013]) are also recorded by the downhole array.

In the same frequency band, some resonance frequencies are simultaneously recorded by the downhole array and two broadband arrays on the surface (A and B). These resonances are intimately related to the fluid injection as the amplitude and the value of the resonances are correlated with variations in slurry flow. On Figure 4, for instance, the spectral lines appear when the injection starts and vanish when it stops.

Throughout the 21 stages, the downhole array presents two main resonances at ~8 and ~11 Hz (Figure 4), plus one at ~4 Hz during the fifth stage of the first well. The amplitude of the resonances is similar at all borehole geophones indicating that the corresponding wavefield is diffuse. Resonance amplitudes are also relatively similar from stage to stage, even for stages 1 km apart. In addition, their apparent velocity is superior to 10 km/s, suggesting that the wavefield is composed of *S* waves propagating nearly horizontally at right angles to the downhole receiver line [*Eaton et al.*, 2013].

3.1.1. Polarization Analysis

Before exploring possible causes of the observed resonance, we calculate the polarization of the continuous recordings on successive segments of 20 s with 50% overlap using the covariance method described by *Jurkevics* [1988] (Figure 5). Prior to the polarization calculation, the microseismic recordings are filtered around the resonance frequencies at 8 Hz using a peak filter in order to select a narrow frequency band (bandwidth ~5–10 Hz). The recordings are rotated in the geographic frame of reference (East-North-Vertical). The polarization measurements during the fluid injection are compared with the polarization of the background noise, obtained from the ~15 min of data before the injection. Only polarization measurements significantly different from those of the background noise are considered hereafter, meaning the analyzed resonance must have sufficient energy.

Figure 5 shows that prior to and after fluid injection, both the incidence angle and azimuth vary considerably. Yet during fluid injection both show a consistent behavior. In particular, there are times when the azimuth varies only within ±10° during a half hour period. The incidence angle shows larger but nonetheless systematic variations. Similar observations are made for different stages and other geophones and broadband seismometers. This indicates that the resonances produce consistent wave propagation patterns.

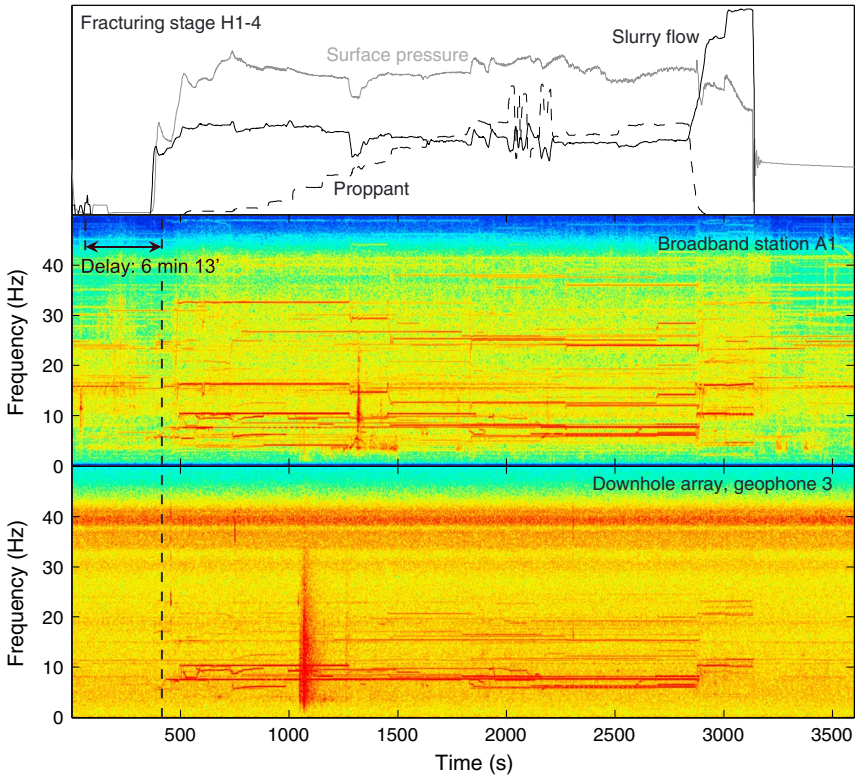

Figure 4. Treatment plot and time-frequency representations of stage H1-4 recorded by the vertical component of broadband station A1 on the surface and downhole geophone 3. The data are downsampled to 100 Hz prior to time-frequency analysis. Hot colors correspond to high amplitudes. Windows of 4 s with 90% overlap are used to compute the time-frequency response. On the treatment plot, the gray line corresponds to surface pressure, the black line to slurry flow, and the dashed line to proppant concentration.

For the downhole array, representative azimuths for both horizontal wells are shown in Figure 6. Azimuths for geophone 4 are similar to the background noise throughout all the stages in well H1. The azimuths are generally in the WSW-ENE direction for both wells, even if the azimuths are slightly more in the direction SW-NE in the case of well H2. The azimuths direction (10–30° [180°]) is roughly perpendicular to the direction injection well-receiver array (~120°).

In the case of the broadband arrays that recorded the same resonances (A and B), the strong contamination of the data by environmental and anthropogenic noises often jeopardizes the polarization measurements. Out of the measurements for all stations and all stages, we carefully selected those which are clearly uncorrupted by strong coherent noises. In Figure 7, we show the average azimuths for the eight stations of the two arrays after this selection. The azimuths are in the SW-NE directions and slightly higher for array A

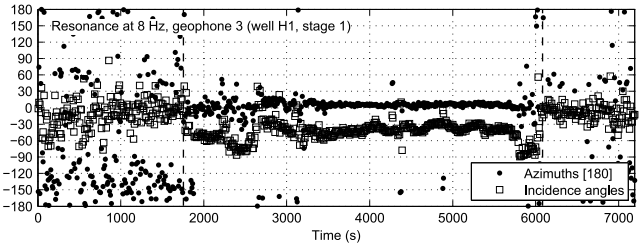

Figure 5. Azimuths and incidence angles for the resonance at 8 Hz and the first stage of the first well as recorded by the third borehole geophone. The 180° ambiguity in the polarization measurements is not removed. The fluid injection starts at 1749 s and stops at 6075 s (vertical dashed lines), corresponding to the part with stable azimuths. Note the oscillations of the incidence angles during the fluid injection.

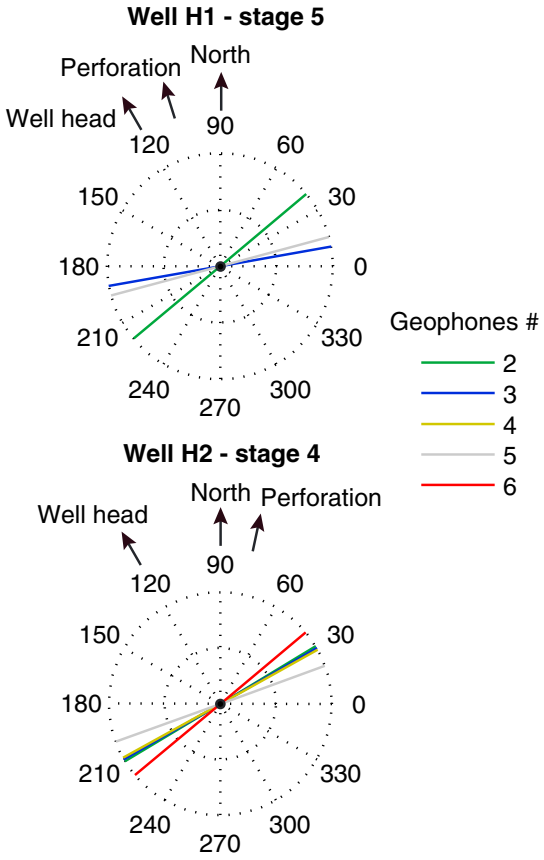

Figure 6. Azimuths corresponding to stages H1-5 and H2-4 after peak filtering the data around 8 Hz. Only the borehole geophones that are not contaminated by background noise are shown. The observation well is located at the center of the rose diagrams. The 180° ambiguity in the polarization measurements is not removed. The general azimuths of the well head of the injection well and the perforation shots (fluid injection) are also indicated on the rose diagrams.

(~70° [180°]) than for array B (~60° [180°]). Overall, the azimuths are perpendicular to the direction injection well-broadband arrays, which is ~140° for array A and ~125° for array B (Figure 7), and the incidence angles are nearly horizontal.

3.1.2. Resonances: Most Likely Cause

3.1.2.1. Receiver Effects

In the following sections, we will separately review each effect to determine their respective influence on our observations. On the receiver side, resonances are mainly generated by the resonance of the borehole or by wave reverberations between the sensors [*St-Onge and Eaton*, 2011]. In the Rolla experiment, the length of the observation well is ~2150 m. If we consider an average cement velocity of 3500 m/s [*Tubman et al.*, 1984], the fundamental frequency associated with this borehole is ~1.6 Hz. Similarly, with a distance between geophones of about 32 m, the corresponding resonance is around 109 Hz [*St-Onge and Eaton*, 2011]. Resonances associated with receiver effects are thus outside the range of the observed resonances.

3.1.2.2. Path Effects

During the Rolla experiment, the resonances were recorded by two different networks. The resonances are visible on different locations but still have the same features, although ray paths are completely different. This is clearly not compatible with path effects. It seems that path and receiver effects for the resonances in common to the downhole and surface arrays can be discarded and then likely related to source effects.

3.1.2.3. Source Effects

The downhole geophones and broadband arrays A and B at the surface have recorded several common resonances. The resonance amplitudes are always higher on the stations of array A than those of array B irrespective of the fracturing stage. In addition, no injection-related resonance was recorded by the other broadband arrays, even though the perforations at the toes of each well are closer to arrays D and G than to arrays A and B (Figure 3).

On the other hand, arrays A and B are closer to the well head of the injection well than the other arrays. The polarization analysis also shows that the azimuths associated with the resonances at 8–11 Hz are consistently perpendicular to the direction injection well-receiver. In the case of the downhole array, it suggests that the resonances are mainly comprised of horizontally polarized S_H waves originating from the vertical part of the injection well, perhaps through the coupling between the pump and the well. For the broadband stations, the resonances could correspond to vibrations produced either directly by the pumping equipment or by the fluid movements in the injection well propagating as S_H or Love waves on the subsurface.

We therefore conclude that for the first case study, the resonances are caused by source side effects. However, they are not representative of vibrations related to the fracture network but most likely caused by the

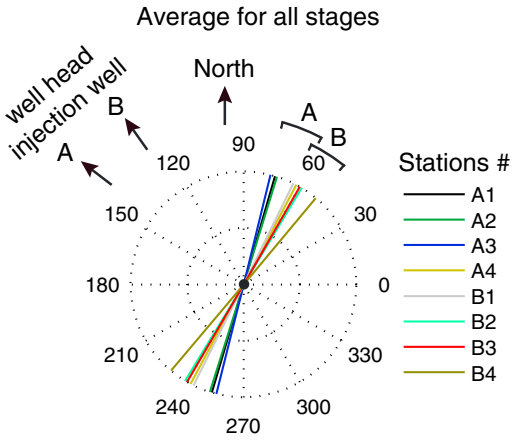

Figure 7. Azimuths for the broadband stations of arrays A and B. The azimuths are averaged over the stages uncorrupted by noises with significant energy in the frequency band around 8 Hz. The directions of the well head of the injection well for both arrays are also indicated.

pumping equipment and/or vibrations within the vertical part of the injection well. The other spectral lines in the surface recordings are likely either harmonics of lower-frequency resonances or noises coming from anthropogenic or environmental sources.

3.2. Case Study 2

The second microseismic experiment is a proprietary data set coming from an anonymous company. During this experiment, fluids (mainly nitrogen and slurry) were injected at depth to increase the permeability of a tight gas reservoir from the Cardium formation. The Cardium formation, belonging to the foreland basin of the Western Canada Sedimentary Basin, results from the flexure of the crust on the western side of the North American Craton during the formation of the Rocky Mountains cordillera [*Wright et al.*, 1994]. As a consequence, the Cardium formation is heavily thrusted and folded. In the study area, the close succession of shales and sandstone could favor the formation of folds between detachments [*Wright et al.*, 1994]. The strikes of folds and thrusts are approximately NW-SE in the region, potentially leading to the formation of compression-related extension fractures perpendicular to the fold strikes and fractures parallel to the fold strikes due to the extension on the fold crests (extrado fractures, [*Hart et al.*, 2007]).

In order to improve the drainage in the Cardium formation, two fracturing stages were monitored by 12 three-component geophones deployed in a vertical borehole (Figure 8). The geophones have a natural frequency of 15 Hz and were sampled at 4000 Hz. A perforation shot is commonly used to break the casing where the fluid injection will take place. These shots are used to determine the orientation of the sensors, using the polarization of the recorded *P* waves [*Jurkevics*, 1988].

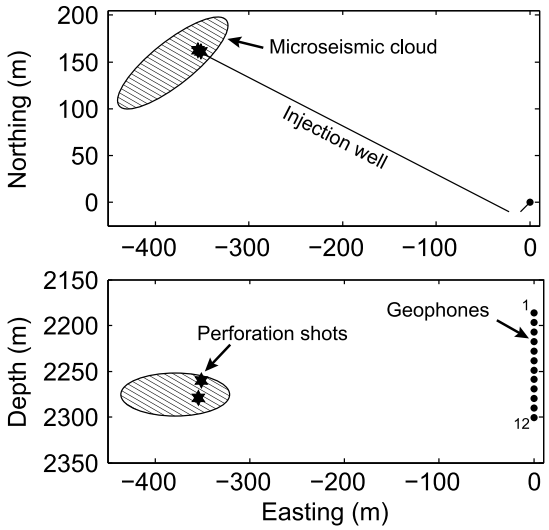

Figure 8. Experimental setup of the second case study, in (top) map view and (bottom) cross-section. The perforation shots are indicated by black stars, the geophones by black dots, and the microseismic cloud by the hatched area. The geophone numbers are also indicated.

The continuous recordings of the two stages show a high-amplitude noise in the frequency band ~15–100 Hz [*Tary and van der Baan*, 2012], hiding completely most of the microseismic events. Only 98 events are located during this experiment with magnitudes ranging from −4 to −3. The microseismic cloud is elongated in the SW-NE direction (Figure 8), parallel to the general compressive direction in the area [*Hart et al.*, 2007].

First-order calculation made by the company to estimate bottom hole slurry flow and treatment pressure for stage 2 indicates that there is a time lag of around 300 s between measures on the surface and at the perforation depth. This is done by applying Darcy's law to the surface treatment data and depends strongly on well layout and fluid properties, in particular, the viscosity and injection pressures, involving some uncertainties in these estimates. Yet to first order, the predicted time lag corresponds to

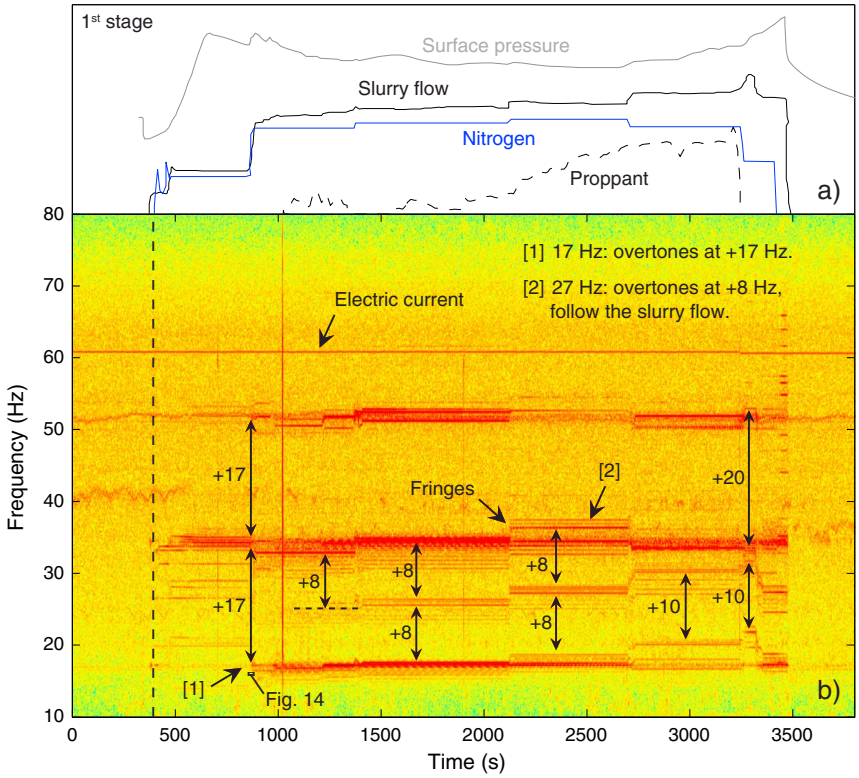

Figure 9. (a) Treatment curves and (b) time-frequency representation of the first stage of the second case study (geophone 12, vertical component). The data are downsampled from 4000 Hz to 160 Hz prior to the time-frequency analysis. Hot colors correspond to high amplitudes. A window of 8 s with 90% overlap are used to compute the short-time Fourier transform. A time shift of +323 s is applied to the treatment curves to align them with the time-frequency representation. In the treatment plot, the gray line = surface pressure, the black line = slurry flow, the blue line = injection rate of nitrogen, and dashed line = proppant concentration.

those applied to the time-frequency representations in order to align variations in frequency and variations in treatment conditions (323 s for stage 1 and 227 s for stage 2).

Several main resonance frequencies are observed during the two stages at ~17, ~35, ~51 and ~60 Hz (Figures 9 and 10) using a short-time Fourier transform. These resonances are confirmed by using a time-varying autoregressive analysis [*Tary et al.*, 2014]. Additional weaker resonances at ~27 Hz during the first stage and at ~16 and ~29 Hz during the second stage are also recorded. Noticeably, the resonance at 27 Hz exhibits numerous fringes around the central spectral lines. The resonance at ~60 Hz corresponds to the electric current. The other resonances at ~17, ~35, and ~51 Hz seem to be harmonics of the resonance at ~17 Hz. They exhibit a particular amplitude pattern, with higher amplitudes on the deepest geophones as well as geophones 4 and 5. Overtones of the additional resonances are also visible. For the first stage, the resonance at 27 Hz is systematically and consistently linked to variations in the resonances at ~17–20, ~32–36, and ~50–53 Hz (Figure 9). Some of them are easily identified by the hat-like feature at ~3400 s, which correlates to a similar feature in the slurry rate. For the second stage, the resonances around 16 and 29 Hz have overtones at ~32 Hz and ~58 Hz, respectively (Figure 10). Overall, the signal energy during both stages is correlated with the fluid flow, meaning that the main source of the background noise is related to the fluid injection. In addition, changes in fluid flow may be correlated with changes in frequency content as mentioned also by *Pettitt et al.* [2009].

In the following, we first analyze the resonance polarizations and moveouts at the geophones and then explore the most likely cause of the resonances. Discussions on the physical interpretation of the changes in frequency are in section 4.

3.2.1. Polarization Analysis

The wavefield corresponding to the resonance at 17 Hz seems to be comprised of transient signals which are coherent across receivers yet are nonetheless highly nonstationary in waveform shape (Figure 11). For

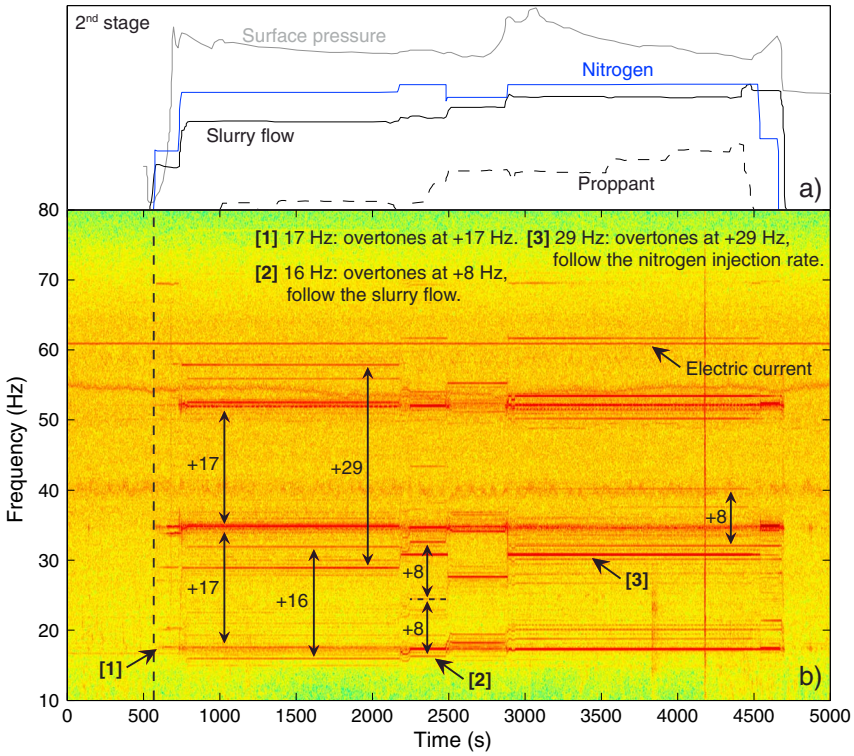

Figure 10. Same as Figure 9 for the second stage of the second case study (geophone 12, vertical component). The time shift applied to the treatment curves is +227 s.

instance, one particular arrival has an apparent moveout of approximately 615 m/s. The corresponding 35 and 51 Hz signals on the other hand display no waveform coherency across multiple receivers.

We apply the same methodology as for the first case study. We computed the polarization for data segments of 25 s with 50% overlap after rotation into the geographic frame of reference and bandpass filtering the seismic trace around the resonance under investigation (bandwidth ~5–10 Hz). Before the fluid injection, the noise in the frequency band around 17 Hz shows sometimes a coherent polarization depending on the geophone. During fluid injection, geophones 4 to 6 and 8 to 12 show a coherent polarization for the first stage, and geophones 4, 5, and 8 to 12 show a coherent polarization for the second stage. In the case of the resonances at ~35 and ~51 Hz, the azimuths are not consistent between stations, but they are in the same direction as the azimuth of the background noise. It suggests that the signal is contaminated by the background noise at these frequencies. In the following, we focus on the interpretation of the resonances and the geophones which are clearly not contaminated by the background noise, i.e., the resonance at 17 Hz recorded by the geophones 4 to 6 and 8 to 12.

The polarization measurements show two main azimuths during both stages. Geophones 4, 11, and 12 show azimuths SW-NE at ~60° [180°], while the other geophones show azimuths to the WNW-ESE at ~150° [180°] (Figure 12). The azimuth SW-NE is perpendicular to the direction observation well-fluid injection and could correspond to *S* waves originating from the fluid injection, whereas the azimuth WNW-ESE is parallel to this direction and could then correspond to *P* waves. The azimuth 285° is also the general direction of a potential source of coherent noise, corresponding to another well located less than 1 km away from the observation well that might be producing at the time of the experiment.

The complex pattern in azimuths and incidence angles between stations may be explained by the local geologic structure. The area is characterized by an ongoing SW-NE compressive regime due to the Cordillera orogeny, involving thrusting and folding of the layers at depth [*Hart et al.*, 2007]. The deformed succession of shale and sandstone layers may create low-velocity waveguides with a complex geometry explaining the complex azimuth pattern observed. Geophones 4, 8, and 9 show high amplitudes on the horizontal components, as well as nearly horizontal incidence angles (Figure 12), suggesting that they are likely located

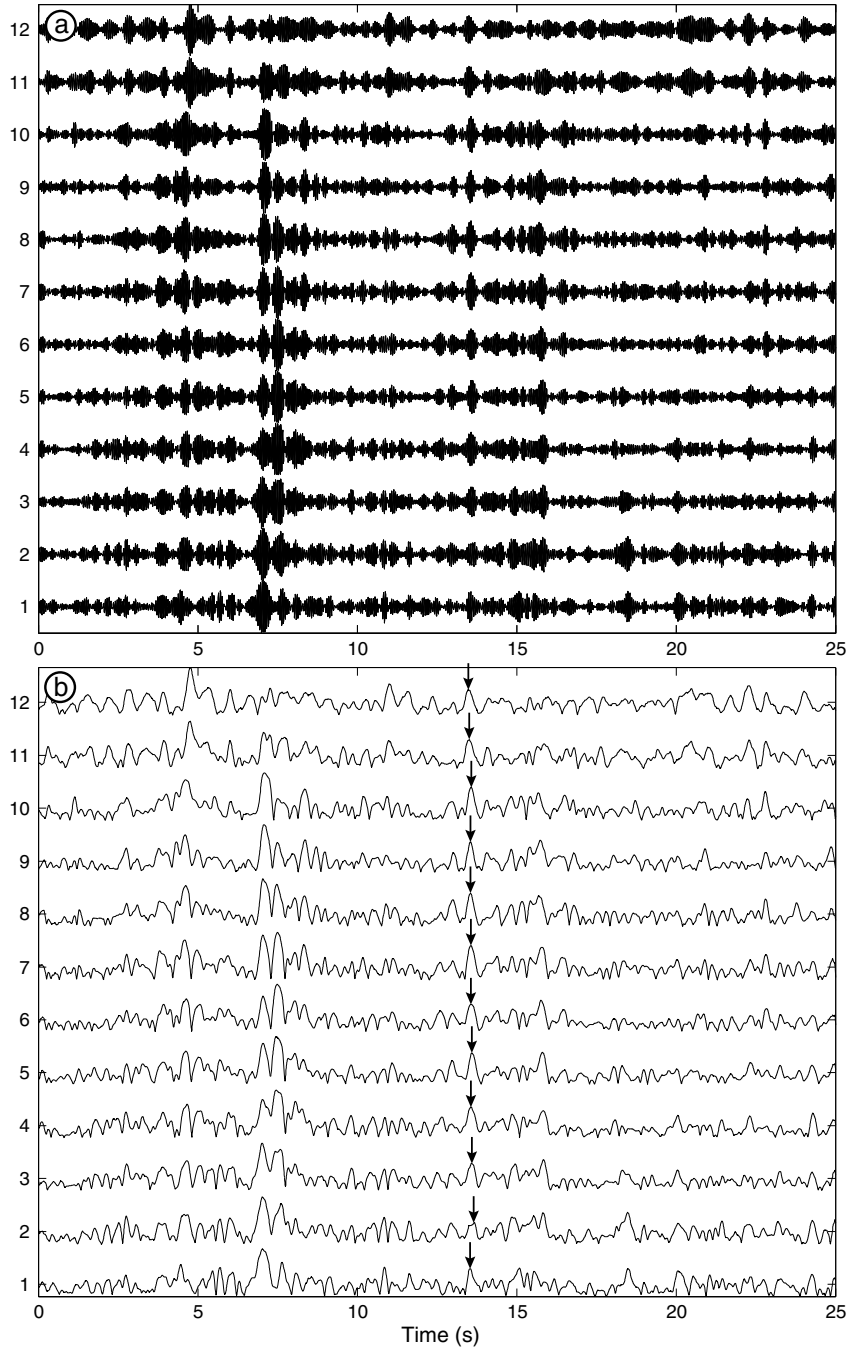

Figure 11. Twenty-five seconds of data from the second stage of the second case study (vertical component of geophones 1 to 12, numbered with increasing depth). (a) Recordings after peak filtering around 17 Hz. (b) Envelope of the signal shown in Figure 11a obtained using the absolute value of the analytic signal. Note the continuity of wave packets between receivers, one of them is indicated by black arrows which has an upward moveout with an apparent velocity of 615 m/s.

close to an interface between 2 layers. On the other hand, the waves arriving at geophones 11 and 12 seem to come from a deeper horizon.

3.2.2. Resonances: Most Likely Cause

3.2.2.1. Receiver Effects

For a ~2300 m long pipe and a *P* wave velocity of the cement casing around 3800 m/s [*Tary and van der Baan*, 2012], the resulting fundamental resonance frequency for the observation well is ~1.7 Hz. Similarly, the resonance frequency corresponding to the spacing between geophones of ~10.4 m is ~365 Hz.

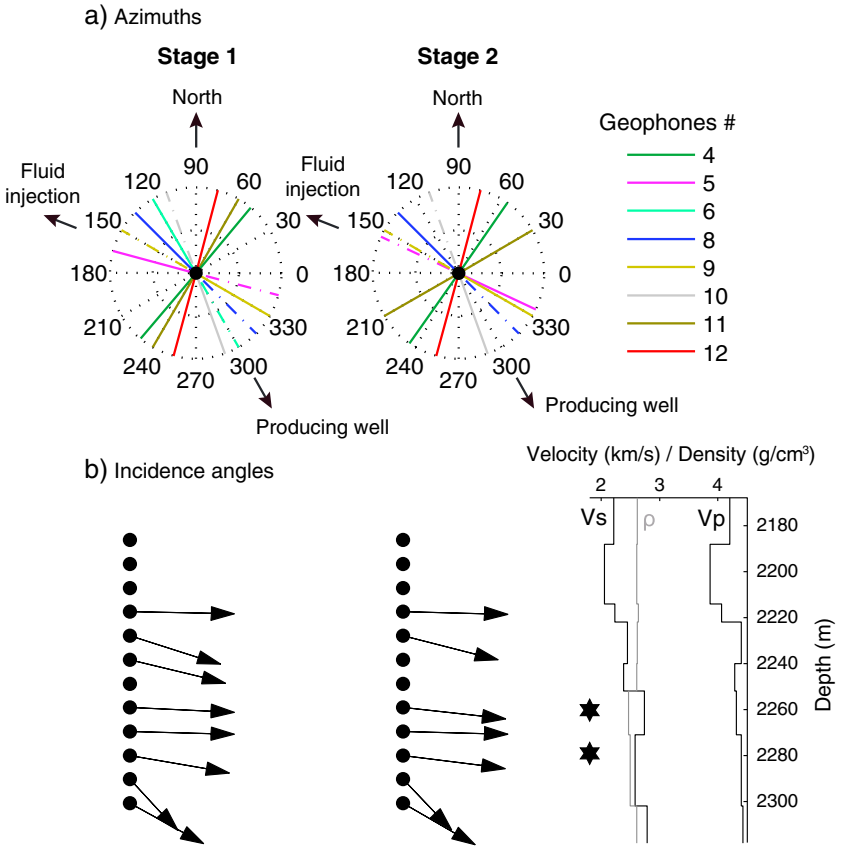

Figure 12. Representative azimuths and incidence angles of the microseismic recordings at a frequency of 17 Hz, for the first and second stages of the second case study. The observation well is located at the center of the rose diagrams. Only the geophones that are not contaminated by background noise are shown. The 180° ambiguity in the polarization measurements is not removed. The general azimuths of the fluid injection and the close-by producing well are also indicated on the rose diagrams. For geophones with azimuths parallel to the direction of fluid injection-receivers, likely related to incident *P* waves, solid line = azimuths along incidence angle, dashed line = complementary angle. The velocity and density (ρ) models used for the wave modeling, as well as the depth of the perforation shots (black stars), are shown in front of the incidence angles using the same depth scale.

These values are out of the range of the observed resonances. In addition, instrument self-noise cannot explain the time variability of the resonances. Surface noises are another option, but they are not consistent with the deepest geophones having higher amplitudes than the shallowest ones and the 17 Hz resonance polarization.

3.2.2.2. Path Effects

In order to determine the influence of path effects and stratigraphic filtering on the frequency content of the microseismic recordings, we perform wave-propagation modeling considering a hypothetic source at the location of the fluid injection (Figure 8). The numerical seismograms are computed using the reflectivity code of *Dietrich* [1988] [*Tary et al.*, 2012]. The source function is a zero-phase Ricker wavelet.

The velocity model (*P* wave and *S* wave), as well as the density structure used for the numerical simulations are based on logs from the injection and observation wells (Figure 12). The same velocity model is used to locate the microseismicity. Different attenuation factors are tested, but their impacts on the simulation outcomes are very limited as the source is only few wavelengths away from the receivers at 17 Hz. Hereafter we use an attenuation factor of 100 for both *P* and *S* waves.

The frequency content of the seismograms, depending on the source-receiver distance, is presented in Figure 13 for three different dominant frequencies (10, 20, and 40 Hz). The source mechanism is a single force in the vertical direction corresponding to mass advection, which could represent momentum transfer by fluid flow in hydraulic stimulations. Changing the source mechanism to horizontal single forces or an isotropic source does not modify significantly the dominant frequency of the numerical seismograms in our

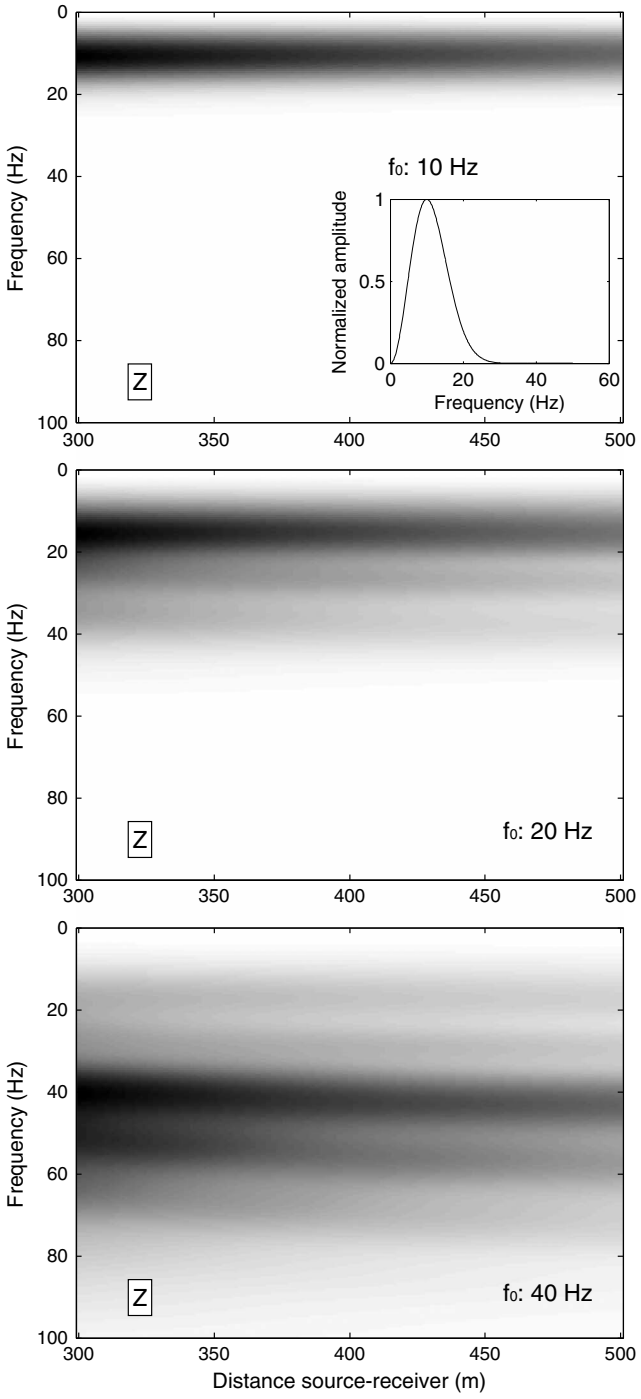

Figure 13. Frequency content versus source-receiver distance for a receiver at the depth of geophone 12 (vertical component), using a source at the location of the deepest perforation shot (~2279 m, see Figure 8), a single force in the vertical direction, and three different dominant frequencies (10, 20, and 40 Hz, see inset). The receiver is located ~400 m away from the source. The frequency content shows little variation with distance, staying very close to the spectrum of the source.

case. The receivers are located approximately at 400 m from the fluid injection. The frequency content of the seismograms stays very similar to the source spectrum, irrespective of the dominant frequency. Recorded wave trains propagate mostly horizontally, limiting the influence of multiple wave scattering as well as wave interferences between wave packets. Little stratigraphic filtering is thus anticipated here.

Ruling out receiver and path effects on the primary generation of the resonance frequencies, we now investigate how source effects could generate the observed resonances.

3.2.2.3. Source Effects

Contrary to the first case study, direct observations of resonances directly related to the pumping equipment are less likely for several reasons. First the strongest resonance amplitudes are recorded on the deepest geophone. Second, the observed moveout in the 17 Hz resonance indicates upward instead of downward wave propagation (Figure 14). Finally, there is a 323 and 227 s lag between the treatment slurry curves and the observed resonances for stages 1 and 2, respectively. Since the physical distance between the pump and the geophones is around 2200 m, this excludes direct wave propagation effects.

On the source side, resonances can thus be generated either by the repetition of small events if perfectly periodic [*Pettitt et al.*, 2009], by the resonance of fluid-filled cracks or by non-Darcian fluid flow in an irregular channel. The stability of the spectral lines throughout the two stages seems to advocate for a stable mechanism that could be either (1) stationary but nonlaminar flow patterns within an open fracture, conditions that could be met close to the injection well, (2) excitation of a crack of stable dimensions and fluid properties, or (3) regular failures at the tip of the growing fracture.

For all models, time delays between the beginning of the fluid injection and the appearance of the resonances are expected due to time needed for the injected fluid to reach the fluid already inside the well and

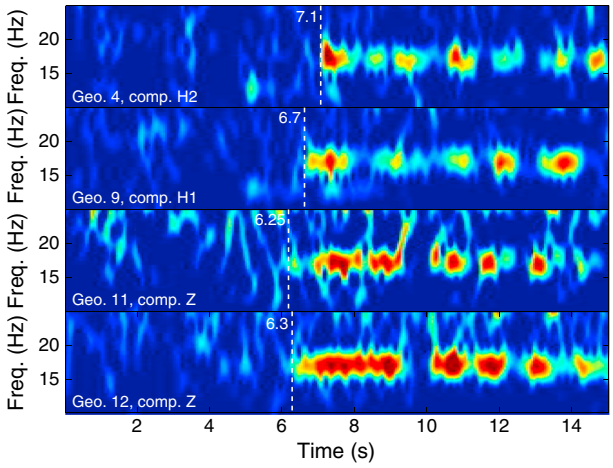

Figure 14. Time-frequency representation (window: 0.5 s, overlap: 90%) centered on the appearance of the resonance at 17 Hz during stage 1 (Figure 9). The four geophones and the component (Z: vertical; H1, H2: horizontal) with the highest amplitude are shown. The time of appearance of the resonance is indicated by white dashed lines.

the reservoir. If we assume linear flow within the well and an average well radius of 10 cm, then it would take fluids in stages 1 and 2 approximately 17.5 and 14.1 min, respectively, to fill-up the 2280 m of the well from the well head to the perforations, given the mean injection rates of 4.1 and 5.1 m^3/min. This is larger than the first order calculation made by the company (300 s) and the observed time lags, but they may be reduced if fluids are already present inside the borehole or due to nonlinear fluid and stress communication between well head and perforation. In addition, contrary to microseismic recordings, start and end points of treatment data are rarely synchronized via GPS but manually timed, introducing a potential source for timing misalignments.

For the first case study, resonances arising from path and receiver effects do not correspond to the observed resonances. They are thus likely caused by source effects at the reservoir's depth. In the next section, we discuss physical interpretations based on the proposed models.

4. Discussion and Implications for Hydraulic Fracturing Mechanisms

In this paper we systematically divide potential causes of resonances into source, receiver, and path effects and subsequently eliminate the least likely ones based on anticipated frequency ranges, signal analysis, and numerical modeling. An improved understanding in the various causes of resonance frequencies and in how to identify the most likely one will aid in a more detailed understanding of their implications for the underlying fluid movements and fracturing mechanisms. For instance, the resonance frequencies in case study 2 (Figures 9 and 10) are nonstationary with some stepwise increases. Does this imply that the fracture network is expanding stepwise or that the resonances respond to fluid flow increases? Is there acceleration in the periodicity with which small repetitive events due to microfracturing occur?

The observed resonances are likely coming from the fluid injection in the reservoir. Shifts in frequency are mainly correlated with fluid flow instead of treatment pressure or proppant volumes. The correlation between fluid flow and resonance frequency is complex, since increases in fluid flow can lead to instantaneous positive or negative shifts in the spectral lines. Complex correlations may reflect the interplay between various physical mechanisms, in particular, since the treatments are a combination of slurry (mostly water combined with viscous thickening agents) and nitrogen injection. The latter is injected as a gaseous phase at the wellhead but turns into a supercritical fluid closer to the reservoir. This leads to significant variations in both viscosity and fluid density along the wellbore as well as within the reservoir and hydraulic fracture. Nonetheless, a correlation between fluid flow and resonance peaks seems clear since both often change in a step-like fashion in line with an instantaneous change in fluid flow, mimicking similar plateaus as well as, for instance, the hat-like feature at the end of the injection in stage 1. For instance, the 27 Hz resonance in stage 1 mimics the slurry flow curve, whereas the 29 Hz resonance in stage 2 seems solely correlated to the variations in nitrogen injection rate instead of the slurry flow.

At the perforation depth (~2300 m), the temperature is ~ 80°C and the fluid pressure is around 55 MPa. In these conditions the nitrogen is in the supercritical state [*Lemmon et al.*, 2013]. The volume fraction of nitrogen at this depth is about 17%. Using the density of nitrogen under these conditions (~374 kg/m^3) and the slurry density (~812 kg/m^3), the density of the fluid is about 738 kg/m^3. The elastic velocities and the density of the medium, coming from the model shown in Figure 12, are averaged over the stimulated reservoir interval: V_p = 4367 m/s, V_s = 2646 m/s, and ρ_m = 2489 kg/m^3. The shear modulus is calculated using

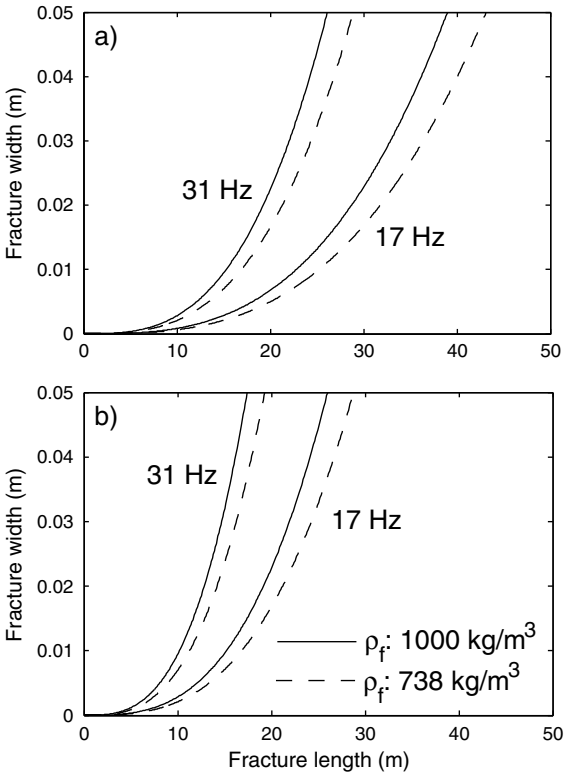

Figure 15. Fracture length versus fracture width corresponding to a fracture (a) with flat tips (equation (A3)) and (b) with the pinch-out model (equation (A6)), for the first mode ($k = 1$), resonance frequencies at 17 and 31 Hz (29 Hz resonance after upward shift at ~2800 s), and fluid densities of 1000 (solid lines) and 738 kg/m^3 (dashed lines). The other parameters are: V_p = 4367 m/s, V_s = 2646 m/s ($\gamma = V_s/V_p$), ρ_m = 2489 kg/m^3, and $\mu = V_s^2\rho_m$ = 17.4 GPa.

$\mu = V_s^2\rho_m$ (~17.4 GPa). The viscosity of the slurry is around 0.025–0.15 Pa s [*Ribeiro and Sharma*, 2012], which is significantly larger than the viscosity of water (0.001 Pa s).

If we assume that the resonances are entirely explained by the excitation of fluid-filled cracks, using expression A3 or A6 and relevant medium properties, we can estimate the dimension of a fracture associated with a specific resonance. For a resonance at 17 Hz and a fracture thickness on the order of the perforation opening (~0.01 m), the fracture is at the limit between thick and thin fracture regimes [*Korneev*, 2008]. In the thick fracture regime, fracture lengths obtained using the aforementioned parameters are around 25 m and 17 m for the flat tips and pinch-out models, respectively (Figure 15). In the thin fracture regime, no such resonance is anticipated as it involves inhomogeneous waves that attenuate very quickly from the interface.

Crack radii corresponding to the magnitude range of microseismic events recorded during microseismic experiments, typically between −3 and −1, range from ~0.25 to ~2 m [*Brune*, 1970]. Compared to a fracture length of 20–30 m, this suggests that a network of interconnected fractures would be required to generate a resonance at 17 Hz. The observed resonances would be caused by wave reverberations within mesoscale interconnected fractures. Nonetheless, the wavefield in geophones 4, 8, and 9 may be somewhat modified by path effects and ray bending, since these are characterized by strong near-horizontal wave motion (Figure 12), yet they record the same resonance frequencies.

Counterarguments rendering the crack excitation model less likely are that over time one would anticipate an expanding hydraulic fracture, producing decreases in resonance frequencies. Specifically, an increase in slurry flow can be thought to produce an acceleration in fracture growth and a decrease may lead to a reduction in fracture growth or possibly even partial fracture closure. Changes in slurry flow and resonance frequencies should then be anticorrelated. However, the opposite is observed in both stages.

For the case of resonances generated by nonlaminar flow, the Reynolds number can be used as an indicator of the flow regime downhole or within the reservoir. At the perforation location, the fluid flow penetrates the reservoir through an opening of the order of 0.01 m. Average fluid flow velocities at the beginning and during the stages inside the borehole coming from the treatment curves are about 1.2 and 2.65 m/s, respectively. Forcing the fluid through an opening of 0.01 m diameter causes a 100-fold increase in the ejection velocities. Combined with a fluid density of 738 kg/m^3 and a dynamic viscosity of 0.1 Pa s, the corresponding Reynolds number are ~8856 and ~19,557. In both cases, inertial forces largely exceed viscous forces which shows that a nonlaminar fluid flow regime is expected at the perforations and inside the reservoir.

Resonance excitation by non-Darcian fluid flow close to the perforation location would be independent of fracture growth or closure over time but directly related to injection rates, thereby explaining the mostly positive correlations between resonance frequencies and treatment rates. This observation points to a model involving non-Darcian flow as the primary cause of the resonance. First-order estimation of the length of the fracture using our parameters and fluid flow models of *Hellweg* [2000] and *Rust et al.* [2008]

give lengths in the order of a few meters for a resonance at 17 Hz. Fluid flow regimes in an expanding fracture network may change over time due to fracture propagation dynamics and potential changes in fluid properties.

Even though the fluid flow model better describes some aspects of the observed correlations, it also raises more questions. For instance, why is the 27 Hz resonance positively correlated to the slurry flow in stage 1, but the similar 29 Hz resonance in stage 2 mimics the N_2 flow? Likewise, nitrogen is combined with slurry to carry proppants into the formation by varying the fluid viscosity. What is the effect of the viscosity on the observed resonances and fluid flow? In addition, hydraulic fracture dimensions and shapes are also likely to influence fluid flow patterns, thus creating potentially complex interactions between crack excitation and flow patterns.

One possible avenue to improve our understanding of what causes the various observed source-related resonances is by studying their variations in amplitudes and quality factors. The quality factor *Q* associated with each resonance, which quantifies the oscillations damping, could help discriminate between different potential causes in some cases. *Q* factors have been used to determine the characteristics of magmatic and hydrothermal fluids because of their high sensitivity to the fluid properties (e.g., density, sound velocity, gas content, presence of solid particles…), and the shape of the resonator [*Nakano et al.*, 1998; *Kumagai and Chouet*, 2000]. For example, an increase in fracture length can be counterbalanced by an increase in fracture width, but the *Q* factor would be different. A thorough comparison between the different properties of resonance frequencies (frequency, amplitude, and *Q* factors) will be treated in future studies.

5. Conclusion

Time-frequency analysis of continuous recordings can play a vital role in unraveling geomechanical effects that happen during fluid injection. In particular, the occurrence of resonance frequencies with variations proportional to the treatment curves contains significant pertinent information. Unfortunately, the presence of a resonance peak in the time-frequency representations does not unambiguously reveal its cause. The framework of separating potential resonances into source, receiver, and path effects greatly aids in understanding the significance of observed spectral peaks. Resonance frequencies can then be used to determine the best fitting model to the observations.

In the first case study, observed resonances are likely due to pumping activities or pumping-fluid-wellbore interactions. For the second case study, the stability of both the resonances and their polarization over the two stages indicates that a localized source of stable dimensions/properties is generating the resonances. Non-Darcian fluid flow models are then more likely owing to the instability of crack jerking due to forced fluid injection. Our conclusions remain qualitative as no comprehensive study exists on the actual behavior of fluid-filled fractures in the context of hydraulic fracturing. In particular, fluids involved in volcano eruptions are very different from those involved in hydraulic fracturing treatments.

A time-frequency analysis complements examination of microseismic event locations and source mechanisms. The microseismic cloud is used by operators to define the approximate area fractured by the fluid. Hence, it represents the reservoir-scale deformation. Microseismic events represent microscale, brittle deformation at the other end of the scale. Resonances could correspond to mesoscale deformation such as interconnected parts of the fracture network. Regarding the energy balance (i.e., total input minus microseismicity energies), these mesoscale deformation could account for a part of the "missing" energy. Resonances are, however, unlikely to account for all the missing energy and may be accompanied by tensile and slow deformation.

We advocate three steps when studying resonances recorded during hydraulic fracturing treatments, (1) accurate determination of time-varying resonances using time-frequency transforms, (2) careful review of possible causes of resonances in each particular cases, and (3) interpretation including general information on the signal characteristics. Hopefully, additional studies of resonance frequencies in different contexts will improve our knowledge of the underlying physical phenomena and our general understanding of geomechanical deformations during fluid injection regardless of whether this is for hydraulic fracturing, CO_2 sequestration, waste water disposal, or volcano seismology.

Appendix A: Resonance Frequencies for Fractures With Flat Tips and Linear Pinch-Out Model

The Krauklis wave is able to sustain the crack resonance, because almost all of its energy is reflected inside the fracture. In addition, its amplitude decreases so rapidly from the sides of the crack that sensors have to be put in close vicinity or inside the fracture to record the wave [*Ferrazzini and Aki*, 1987; *Tang and Cheng*, 1988]. The wavefield that is actually recorded during magma and fluid injection comes from the diffraction of the Krauklis wave at the tips of the cracks [*Groenenboom and Fokkema*, 1998; *Groenenboom and Falk*, 2000; *Frehner and Schmalholz*, 2010].

The viscosity of the fluid inside the crack does not have a significant effect on the phase velocity of Krauklis waves when the crack is wide enough ("thick fracture regime" of *Korneev* [2008]), or for fluids with a low viscosity such as water or oil [*Chouet*, 1986; *Frehner and Schmalholz*, 2010]. In this case, the low-frequency asymptote of the phase velocity of Krauklis waves is given by [*Korneev*, 2008]

$$V_K = \sqrt[3]{\frac{h\mu f}{\rho_f}(1-\gamma^2)} \tag{A1}$$

where f is the frequency, h is the fracture width, μ is the shear modulus of the solid, ρ_f is the density of the fluid inside the crack, and γ is the ratio in elastic velocities of the solid (V_s/V_p).

At low frequencies (5–100 Hz), wavelengths associated with the Krauklis wave are about few meters to few tens of meters. Hence, openings due to other cracks (few millimeters) or the borehole ($\sim$ 10 cm) are very small compared to the Krauklis wave wavelength. We consider therefore that the entire system is adequately represented as a closed fracture with rigid tips. The resonant condition in this case corresponds to

$$l = \lambda_k \frac{k}{2}, \qquad k = 1, 2, 3, \ldots \tag{A2}$$

where l is the fracture length, λ_k the wavelength of kth mode ($\lambda_k = \frac{2\pi V_K}{f_k}$). Using equations (A1) and (A2), the resonance frequency for a fracture with flat tips is given by

$$f_k = \sqrt{\frac{h\mu\pi^3 k^3}{l^3\rho_f}(1-\gamma^2)}, \qquad k = 1, 2, 3, \ldots . \tag{A3}$$

Fracture tips usually pinch-out progressively rather than being flat [*Rubin*, 1995]. In this case, the phase velocity of the Krauklis wave decreases toward the tip of the fracture [*Frehner and Schmalholz*, 2010], increasing the travel time in the fracture. Assuming a linear decrease of the fracture thickness at the tip, a fracture with length l reaching a maximum thickness h_0 at the tip has a thickness at distance x given by $h = h_0\frac{x}{l}$. With $T_0 = \frac{l}{V_K}$, the travel time for a uniform fracture, the phase velocity of the Krauklis wave in the pinch-out fracture is

$$\widetilde{V}_K = \sqrt[3]{\frac{h\mu f}{\rho_f}(1-\gamma^2)} = V_K\sqrt[3]{\frac{h}{h_0}} = \frac{l}{T_0}\sqrt[3]{\frac{x}{l}}, \tag{A4}$$

and the corresponding travel time is

$$T = \int_0^l \frac{\mathrm{d}x}{\widetilde{V}_K} = T_0\frac{\sqrt[3]{l}}{l}\int_0^l \frac{\mathrm{d}x}{\sqrt[3]{x}} = T_0\int_0^1 \frac{\mathrm{d}x}{\sqrt[3]{x}} = \frac{3}{2}T_0. \tag{A5}$$

Taking into account this increase in travel time, the resonance frequency given by equation (A3) becomes

$$\widetilde{f}_k = \sqrt{\frac{8}{27}\frac{h\mu\pi^3 k^3}{l^3\rho_f}(1-\gamma^2)}, \qquad k = 1, 2, 3, \ldots . \tag{A6}$$

Acknowledgments
The authors would like to thank the sponsors of the Microseismic Industry consortium for financial support and an anonymous company for permission to show and use their data. Arc Resources, Nanometrics, and ESG Solutions are particularly thanked for their support of the field project of the Rolla experiment. We thank Bruce Sutherland for discussions on the generation of resonances by nonlaminar fluid flow. Constructive reviews by two anonymous reviewers and particularly Valeri Korneev greatly improved the original manuscript.

References

Aki, K., M. Fehler, and S. Das (1977), Source mechanism of volcanic tremors: Fluid-driven crack model and their application to the 1963 Kilauea eruption, *J. Volcanol. Geotherm. Res.*, *2*(3), 259–287, doi:10.1016/0377-0273(77)90003-8.

Bame, D., and M. Fehler (1986), Observations of long period earthquakes accompanying hydraulic fracturing, *Geophys. Res. Lett.*, *13*(1), 149–152, doi:10.1029/GL013i002p00149.

Banik, N. C., I. Lerche, J. R. Resnick, and R. T. Shuey (1985), Stratigraphic filtering, Part II: Model spectra, *Geophysics*, *50*(12), 2775–2783, doi:10.1190/1.1441898.

Bohnhoff, M., and M. D. Zoback (2010), Oscillation of fluid-filled cracks triggered by degassing of CO_2 due to leakage along wellbores, *J. Geophys. Res.*, *115*, B11305, doi:10.1029/2010JB000848.

Bonnefoy–Claudet, S., F. Cotton, and P.-Y. Bard (2006), The nature of noise wavefield and its applications for site effects studies: A literature review, *Earth Sci. Rev.*, *79*(3-4), 205–227, doi:10.1016/j.earscirev.2006.07.004.

Brune, J. N. (1970), Tectonic stress and the spectra of seismic shear waves from earthquakes, *J. Geophys. Res.*, *75*(26), 4997–5009, doi:10.1029/JB075i026p04997.

Burlini, L., S. Vinciguerra, G. Di Toro, G. De Natale, P. Meredith, and J.-P. Burg (2007), Seismicity preceding volcanic eruptions: New experimental insights, *Geology*, *35*(2), 183–186, doi:10.1130/G23195A.1.

Calo, M., C. Dorbath, F. H. Cornet, and N. Cuenot (2011), Large-scale aseismic motion identified through 4-D P-wave tomography, *Geophys. J. Int.*, *186*(3), 1295–1314, doi:10.1111/j.1365-246X.2011.05108.x.

Chopra, S., L. Lines, D. R. Schmitt, and M. Batzle (2010), Heavy-oil reservoirs: Their characterization and production, in *Heavy Oils: Reservoir Characterization and Production Monitoring*, edited by S. Chopra et al., Society of Exploration Geophysicists, Tulsa.

Chorney, D., P. Jain, M. Grob, and M. van der Baan (2012), Geomechanical modeling of rock fracturing and associated microseismicity, *Leading Edge*, *31*(11), 1348–1354, doi:10.1190/tle311113481.

Chouet, B. (1986), Dynamics of a fluid-driven crack in three dimensions by the finite difference method, *J. Geophys. Res.*, *91*(B14), 13,967–13,992, doi:10.1029/JB091iB14p13967.

Chouet, B. (1988), Resonance of a fluid-driven crack: Radiation properties and implications for the source of long-period events and harmonic tremor, *J. Geophys. Res.*, *93*(B5), 4375–4400, doi:10.1029/JB093iB05p04375.

Chouet, B., P. Dawson, and A. Arciniega-Ceballos (2005), Source mechanism of vulcanian degassing at Popocatépetl Volcano, Mexico, determined from waveform inversions of very long period signals, *J. Geophys. Res.*, *110*, B07301, doi:10.1029/2004JB003524.

Correig, A. M., and J. Vila (1993), On the frequency content of local events: Source or path effects?, *Geophys. J. Int.*, *115*(3), 863–877, doi:10.1111/j.1365-246X.1993.tb01498.x.

Das, I., and M. D. Zoback (2011), Long-period, long-duration seismic events during hydraulic fracture stimulation of a shale gas reservoir, *Leading Edge*, *30*(7), 778–786, doi:10.1190/1.3609093.

Das, I., and M. D. Zoback (2013), Long-period, long-duration seismic events during hydraulic stimulation of shale and tight-gas reservoirs—Part 1: Waveform characteristics, *Geophysics*, *78*(6), KS107–KS118, doi:10.1190/GEO2013-0164.1.

De Barros, L., I. Lokmer, C. J. Bean, G. S. O'Brien, G. Saccorotti, J.-P. Métaxian, L. Zuccarello, and D. Patanè (2011), Source mechanism of long-period events recorded by a high-density seismic network during the 2008 eruption on Mount Etna, *J. Geophys. Res.*, *116*, B01304, doi:10.1029/2010JB007629.

de Ridder, S., and J. Dellinger (2011), Ambient seismic noise eikonal tomography for near-surface imaging at Valhall, *Leading Edge*, *30*(5), 506–512, doi:10.1190/1.3589108.

Dietrich, M. (1988), Modeling of marine seismic profiles in the t-x and τ-p domains, *Geophysics*, *53*(4), 453–465, doi:10.1190/1.1442477.

Dixon, J. (2000), Regional lithostratigraphic units in the Triassic Montney Formation of western Canada, *Bull. Can. Petrol. Geol.*, *48*(1), 80–83, doi:10.2113/48.1.80.

Eaton, D., M. van der Baan, J. B. Tary, B. Birkelo, N. Spriggs, S. Cutten, and K. Pike (2013), Broadband microseismic observations from a Montney hydraulic fracture treatment, northeastern B. C., Canada, *CSEG Recorder*, *38*(3), 44–53.

Eaton, D. W., M. van der Baan, B. Birkelo, and J.-B. Tary (2014), Scaling relations and spectral characteristics of tensile microseisms: Evidence for opening/closing cracks during hydraulic fracturing, *Geophys. J. Int.*, doi:10.1093/gji/ggt498, (to appear in print).

Evans, K. F., T. Kohl, R. J. Hopkirk, and L. Rybach (1996), Studies of the nature of non-linear impedance to flow within the fractured granitic reservoir at the European Hot Dry Rock project site, Bundesamt für Bildung & Wissenschaft, Bern, Switzerland.

Ferrazzini, V., and K. Aki (1987), Slow waves trapped in a fluid-filled infinite crack: Implication for volcanic tremor, *J. Geophys. Res.*, *92*(B9), 9215–9223, doi:10.1029/JB092iB09p09215.

Ferrazzini, V., B. Chouet, M. Fehler, and K. Aki (1990), Quantitative analysis of long-period events recorded during hydrofracture experiments at Fenton Hill, New Mexico, *J. Geophys. Res.*, *95*(B13), 21,871–21,884, doi:10.1029/JB095iB13p21871.

Ferrick, M. G., A. Qamar, and W. F. St. Lawrence (1982), Source mechanism of volcanic tremor, *J. Geophys. Res.*, *87*(B10), 8675–8683, doi:10.1029/JB087iB10p08675.

Frehner, M., and S. M. Schmalholz (2010), Finite-element simulations of Stoneley guided–waves reflection and scattering at the tips of fluid-filled fractures, *Geophysics*, *75*(2), T23–T36, doi:10.1190/1.3340361.

Goloshubin, G. M., P. V. Krauklis, L. A. Molotkov, and H. B. Helle (1994), Slow wave phenomenon at seismic frequencies, *Paper presented at SEG 63rd Annual International Meeting,* Washington, D. C.

Grechka, V., and Y. Zhao (2012), Microseismic interferometry, *Leading Edge*, *31*(12), 1478–1483, doi:10.1190/tle311214781.

Groenenboom, J., and J. Falk (2000), Scattering by hydraulic fractures: Finite difference modeling and laboratory data, *Geophysics*, *65*(2), 612–622, doi:10.1190/1.1444757.

Groenenboom, J., and J. T. Fokkema (1998), Guided waves along hydraulic fractures, *Paper presented at SEG 67th Annual International Meeting,* New Orleans, La.

Hart, B. S., B. L. Varban, K. J. Marfurt, and A. G. Plint (2007), Blind thrusts and fault-related folds in the Upper Cretaceous Alberta Group, deep basin, west-central Alberta: Implications for fractured reservoirs, *Bull. Can. Petrol. Geol.*, *55*(2), 125–137, doi:10.2113/gscpgbull.55.2.125.

Hellweg, M. (2000), Physical models for the source of Lascar's harmonic tremor, *J. Volcanol. Geotherm. Res.*, *101*(1-2), 183–198, doi:10.1016/S0377-0273(00)00163-3.

Hotovec, A. J., S. G. Prejean, J. E. Vidale, and J. Gomberg (2013), Strongly gliding harmonic tremor during the 2009 eruption of Redoubt Volcano, *J. Volcanol. Geotherm. Res.*, *259*, 89–99, doi:10.1016/j.jvolgeores.2012.01.001.

Julian, B. R. (1994), Volcanic tremor: Nonlinear excitation by fluid flow, *J. Geophys. Res.*, *99*(B6), 11,859–11,877, doi:10.1029/93JB03129.

Jurkevics, A. (1988), Polarization analysis of three-component array data, *Bull. Seismol. Soc. Am.*, *78*(5), 1725–1743.

Konstantinou, K. I., and V. Schlindwein (2003), Nature, wavefield properties and source mechanism of volcanic tremor: A review, *J. Volcanol. Geotherm. Res.*, *119*(1-4), 161–187, doi:10.1016/S0377-0273(02)00311-6.

Kohl, T., K. F. Evans, R. J. Hopkirk, R. Jung, and L. Rybach (1997), Observation and simulation of non-Darcian flow transients in fractured rock, *Water Resour. Res.*, *33*(3), 407–418.
Korneev, V. (2008), Slow waves in fractures filled with viscous fluid, *Geophysics*, *73*(1), N1–N7, doi:10.1190/1.2802174.
Korneev, V. (2011), Krauklis wave in a stack of alternating fluid-elastic layers, *Geophysics*, *76*(6), N47–N53, doi:10.1190/geo2011-0086.1.
Kumagai, H., and B. Chouet (2000), Acoustic properties of a crack containing magmatic or hydrothermal fluids, *J. Geophys. Res.*, *105*(B11), 25,493–25,512, doi:10.1029/2000JB900273.
Lees, J. M., E. I. Gordeev, and M. Ripepe (2004), Explosions and periodic tremor at Karymsky volcano, Kamchatka, Russia, *Geophys. J. Int.*, *158*(3), 1151–1167, doi:10.1111/j.1365-246X.2004.02239.x.
Lemmon, E. W., M. O. McLinden, and D. G. Friend (2013), Thermophysical properties of fluid systems, in *NIST Chemistry WebBook, NIST Standard Reference Database Number 69*, edited by P. J. Linstrom and W. G. Mallard, National Institute of Standards and Technology, Gaithersburg MD, 20899. http://webbook.nist.gov, (retrieved August 23, 2013).
Lesage, P., M. M. Mora, G. E. Alvarado, J. Pacheco, and J.-P. Métaxian (2006), Complex behavior and source model of the tremor at Arenal volcano, Costa Rica, *J. Volcanol. Geotherm. Res.*, *157*(1-3), 49–59, doi:10.1016/j.jvolgeores.2006.03.047.
Maeda, Y., H. Kumagai, R. Lacson Jr., M. S. Figueroa II, and T. Yamashina (2013), Source process of long-period seismic events at Taal volcano, Philippines: Vapor transportation and condensation in a shallow hydrothermal fissure, *J. Geophys. Res. Solid Earth*, *118*, 2832–2846, doi:10.1002/jgrb.50205.
Maxwell, S. C., J. Du, J. Shemeta, U. Zimmer, N. Boroumand, and L. G. Griffin (2007), Monitoring SAGD steam injection using microseismicity and tiltmeters, *Paper presented at the SPE Annual Technical Conference and Exhibition, SPE 1106634,* Anaheim, Calif.
Maxwell, S. C., J. Shemeta, E. Campbell, and D. Quirk (2009), Microseismic deformation rate monitoring, *Paper presented at EAGE Passive Seismic Workshop,* Limassol, Cyprus.
Morlet, J., G. Arens, E. Fourgeau, and D. Giard (1982a), Wave propagation and sampling theory: Part I. Complex signal and scattering in multilayered media, *Geophysics*, *47*(2), 203–221, doi:10.1190/1.1441328.
Morlet, J., G. Arens, E. Fourgeau, and D. Giard (1982b), Wave propagation and sampling theory: Part II. Sampling theory and complex waves, *Geophysics*, *47*(2), 222–236, doi:10.1190/1.1441329.
Nagano, K., and H. Niitsuma (2000), Dispersion analysis of crack-waves in an artificial subsurface fracture using two crack models, *IEEE Trans. Geosci. Remote Sens.*, *38*(1), 3–11.
Nakano, M., H. Kumagai, M. Kumazawa, K. Yamaoka, and B. A. Chouet (1998), The excitation and characteristic frequency of the long-period volcanic event: An approach based on an inhomogeneous autoregressive model of a linear dynamic system, *J. Geophys. Res.*, *103*(B5), 10,031–10,046, doi:10.1029/98JB00387.
Nakamura, Y. (2000), Clear identification of fundamental idea of Nakamura's technique and its applications, *Proceedings of the XII World Conference Earthquake Engineering,* New Zealand, Paper no. 2656.
National Energy Board (2009), A primer for understanding Canadian shale gas. Accessed online at http://www.neb.gc.ca/clf–nsi/rnrgynfmtn/nrgyrprt/ntrlgs/ prmrndrstndngshlgs2009/prmrndrstndngshlgs2009-eng.pdf on March 3, 2013.
Neuberg, J. W., H. Tuffen, L. Collier, D. Green, T. Powell, and D. Dingwell (2006), The trigger mechanism of low-frequency earthquakes on Montserrat, *J. Volcanol. Geotherm. Res.*, *153*(1-2), 37–50, doi:10.1016/j.jvolgeores.2005.08.008.
Pettitt, W., J. Reyes-montes, B. Hemmings, E. Hughes, and R. P. Young (2009), Using continuous microseismic records for hydrofracture diagnostics and mechanics, *Paper presented at SEG 79th Annual International Meeting,* Houston, Tex.
Quinn, P. M., J. A. Cherry, and B. L. Parker (2011), Quantification of non-Darcian flow observed during packer testing in fractured sedimentary rock, *Water Resour. Res.*, *47*, W09533, doi:10.1029/2010WR009681.
Rama Rao, V. N., and J. K. Vandiver (1999), Acoustics of fluid-filled boreholes with pipe: Guided propagation and radiation, *J. Acoust. Soc. Am.*, *105*(6), 3057–3066, doi:10.1121/1.424635.
Ribeiro, L. H., and M. M. Sharma (2012), Multiphase fluid-loss properties and return permeability of energized fracturing fluids, *SPE Prod. Oper.*, *27*(3), 265–277, SPE-139622-PA, doi:10.2118/139622-PA.
Rubin, A. (1995), Propagation of magma-filled cracks, *Annu. Rev. Earth Planet. Sci.*, *23*, 287–336, doi:10.1146/annurev.ea.23.050195.001443.
Rust, A. C., N. J. Balmforth, and S. Mandre (2008), The feasibility of generating low-frequency volcano seismicity by flow through a deformable channel, *Geol. Soc. London, Spec. Publ.*, *307*, 45–56, doi:10.1144/SP307.4.
Shimomura, Y., T. Nishimura, and H. Sato (2006), Bubble growth processes in magma surrounded by an elastic medium, *J. Volcanol. Geotherm. Res.*, *155*(3-4), 307–322, doi:10.1016/j.jvolgeores.2006.04.003.
St-Onge, A., and D. W. Eaton (2011), Noise examples from two microseismic datasets, *CSEG Recorder*, *36*(10), 46–49.
St-Onge, A., D. W. Eaton, and A. Pidlisecky (2013), Borehole vibration response to hydraulic fracture pressure, paper presented at CSEG Geoconvention, Calgary.
Sun, R., and G. A. McMechan (1988), Finite-difference modeling of borehole resonances, *Energy Sources*, *10*(1), 55–75, doi:10.1080/00908318808908916.
Tang, X. M., and C. H. Cheng (1988), Wave propagation in a fluid-filled fracture—An experimental study, *Geophys. Res. Lett.*, *15*(13), 1463–1466, doi:10.1029/GL015i013p01463.
Tary, J. B., L. Géli, C. Guennou, P. Henry, N. Sultan, N. Çağatay, and V. Vidal (2012), Microevents produced by gas migration and expulsion at the seabed: A study based on sea bottom recordings from the Sea of Marmara, *Geophys. J. Int.*, *190*(2), 993–1007, doi:10.1111/j.1365-246X.2012.05533.x.
Tary, J. B., R. H. Herrera, and M. van der Baan (2014), Time-varying autoregressive model for spectral analysis of microseismic experiments and long-period volcanic events, *Geophys. J. Int.*, *196*(1), 600–611, doi:10.1093/gji/ggt400.
Tary, J. B., and M. van der Baan (2012), Potential use of resonance frequencies in microseismic interpretation, *Leading Edge*, *31*(11), 1338–1346, doi:10.1190/tle311113381.
Thomas, M. E., and J. Neuberg (2012), What makes a volcano tick—A first explanation of deep multiple seismic sources in ascending magma, *Geology*, *40*(4), 351–354, doi:10.1130/G32868.1.
Tubman, K. M., C. H. Chang, and M. N. Toksöz (1984), Synthetic full waveform acoustic logs in cased boreholes, *Geophysics*, *49*(7), 1051–1059, doi:10.1190/1.1441720.
van der Baan, M., J. Wookey, and D. Smit (2007), Stratigraphic filtering and source penetration depth, *Geophys. Prospect.*, *55*(5), 679–684, doi:10.1111/j.1365-2478.2007.00647.x.
van der Baan, M. (2001), Acoustic wave propagation in one-dimensional random media: The wave localization approach, *Geophys. J. Int.*, *145*(3), 631–646, doi:10.1046/j.1365-246x.2001.01405.x.
van der Baan, M. (2009), The origin of SH-wave resonance frequencies in sedimentary layers, *Geophys. J. Int.*, *178*(3), 1587–1596, doi:10.1111/j.1365-246X.2009.04245.x.

van der Baan, M., D. Eaton, and M. Dusseault (2013), Microseismic monitoring developments in hydraulic fracture stimulation, in *Effective and Sustainable Hydraulic Fracturing*, edited by R. Jeffrey et al., InTech, Rijeka, Croatia, 439–466, doi:10.5772/56444, (to appear in print).

Van Dyke, M. (1982), *An Album of Fluid Motion*, The Parabolic Press, Stanford, Calif.

Wright, G. N., M. E. McMechan, and D. E. G. Potter (1994), Structure and architecture of the Western Canada sedimentary basin, in *Geological Atlas of the Western Canada Sedimentary Basin*, edited by G. D. Mossop and I. Shetsen, Canadian Society of Petroleum Geologists and Alberta Research Council, Calgary. Accessed online at http://www.ags.gov.ab.ca/publications/wcsb_atlas/atlas.html on April 3, 2013.

Yamamoto, M., and H. Kawakatsu (2008), An efficient method to compute the dynamic response of a fluid-filled crack, *Geophys. J. Int.*, *174*(3), 1174–1186, doi:10.1111/j.1365-246X.2008.03871.x.

Zonneveld, J.-P., R. B. MacNaughton, J. Utting, T. W. Beatty, S. G. Pemberton, and C. M. Henderson (2010), Sedimentology and ichnology of the Lower Triassic Montney Formation in the Pedigree-Ring/Border-Kahntah River area, northwestern Alberta and northeastern British Columbia, *Bull. Can. Petrol. Geol.*, *58*(2), 115–140, doi:10.2113/gscpgbull.58.2.115.